Thomson scattering-induced bandgap in planar chiral phononic crystals

Wei Ding, Tianning Chen, Chen Chen, Dimitrios Chronopoulos, Jian Zhu, Badreddine Assouar

Thomson Scattering-induced Bandgap in Planar Chiral Phononic Crystals

Wei Ding[1], Tianning Chen[1], Chen Chen[1], Dimitrios Chronopoulos[2], Jian Zhu[1,3]*, Badreddine Assouar[4]*

[1]*School of Mechanical Engineering and State Key Laboratory of Strength & Vibration of Mechanical Structures, Xi'an Jiaotong University, Xi'an, Shaanxi 710049, P.R. China*

[2]*Department of Mechanical Engineering & Mechatronic System Dynamics (LMSD), KU Leuven, 9000, Belgium*

[3]*School of Mechanical Engineering and State Key Lab of Digital Manufacturing Equipment & Technology, Huazhong University of Science and Technology, Wuhan, Hubei, 430074, P. R. China*

[4]*Université de Lorraine, CNRS, Institut Jean Lamour, F-54000 Nancy, France*

**E-mail: jianzhuxj@xjtu.edu.cn; badreddine.assouar@univ-lorraine.fr*

Abstract

Releasing the dependence of the low-frequency and broad bandgaps on low stiffness and bulky masses has been an intractable bottleneck. Although inertial amplification is a terrific candidate for addressing the barrier, numerous extended ideas are limited to the classical models, thus, slowing or stalling the advances in this demand. To break this limit, we report a kind of planar chiral phononic crystal based on Thomson scattering. Different from the optimization effect produced in the locally resonant phononic crystals, the mirrored chirality can open a Thomson scattering-induced broad bandgap when the local resonant sub-structure is discarded. In addition, while simplifying the material components, we lower the starting frequency of the bandgap with a virtually unchanged width for the same lattice constant, stiffness and mass. Consequently, the starting frequency of the attenuation can be in the same order of magnitude as the local resonance bandgap, while the width is significantly better than the latter. Our proposal may open a new way to manipulate broadband elastic waves and validate that Thomson scattering is a promising alternative approach and mechanism for bandgap formation.

1. Introduction

Chirality, i.e., the spatial arrangement which does not possess centrosymmetry and rotational symmetry [1-3], makes macroscopic materials with negative Poisson's ratio effects [4-6]. In essence, the rotation-translation coupling in these lattices is the fundamental basis of the negative Poisson's ratio [6, 7]. Therefore, both axial and planar twist chiral lattices can achieve this unique property [8, 9].

Chirality in geometry can not only endow mechanical metastructures with negative Poisson's ratio as well as twist [10-13], but also can produce phononic crystals (or elastic metastructures) with some unique dynamical properties, such as elastic wave polarization [14-18], nonlinear wave propagation[19], enhancing stiffness and damping [20, 21], widening local resonance-induced bandgap [22-26]. At present, the planar chiral lattice has been received intensive investigations [27]. In these researches, the coupling of the translation and rotation can generate a positive elastic module [28, 29], and embedding locally resonant substructure can achieve negative dynamic equivalent density [29-31]. When the double negative properties overlap in the same frequency band, it is beneficial to achieve negative refraction [28, 31, 32]. However, the double negative properties are unbeneficial for opening a continuous bandgap due to the pass band with negative group velocity induced by the negative elastic module [29, 31]. Therefore, using chiral lattices to create a broad local resonance-induced bandgap mainly depends on the excellent stiffness-mass ratio (specific stiffness) of the matrix [20, 22, 27, 33]. It is well known that the lower boundary of the local resonance bandgap is negatively correlated with the ratio of the oscillator and matrix masses [24, 34, 35], while the bandwidth of the negative dynamic equivalent density is positively correlated with the ratio of the oscillator to the substrate mass [30, 36]. Therefore, improving the specific stiffness of the matrix can optimize the local resonance-induced bandgap.

In axial twist chiral phononic crystals [37-39], motion coupling is a critical factor in bandgap formation [40]. At deep subwavelength scales, because of this coupling, the outgoing wave will propagate in two polarization modes when the incident wave polarized in one mode propagates through this chiral substructure. This progress is analogous to Thomson scattering in classical electromagnetic fields. In classical Thomson scattering, the incident wave forces the electron to vibrate, thus generating a divergent wave field. The divergent outgoing field results from superimposing waves polarized in multiple directions [40]. In this analogy, the chiral sub-unit cell is regarded as the electron; the two and more waves polarized in different freedoms were superimposed to form an outgoing wave field [40].

More critically, a phononic crystal with the Thomson scattering-induced bandgap must have a second Thomson scattering ability to cause destructive interferences [40]. Specifically, two polarization modes are produced through the first Thomson scattering. After that, the scattered waves vibrating in these two modes each take on the role of secondary incident waves for a second Thomson scattering. These second scattered

waves polarized in the same mode will have opposite phases, and thus cause destructive interferences [40]. During the quantification of the analogous Thomson scattering, the inertia matrix will show the inertial amplification effect [41-43]. It has been demonstrated that the geometric and physical parameters, including lattice constant, equivalent stiffness, and density, are inextricably linked to the starting frequency and width of the bandgap [44-46]. Because of the inertial amplification [37, 39], whose dynamic inertia can be amplified without increasing the static inertia, theoretically, this bandgap can be lower than Bragg scattering for the same lattice constant, equivalent density, and stiffness [41, 47], and this lattice will be lighter than the local resonance lattice for the same lattice constant, equivalent stiffness and bandgap width requirements [41, 47-49]. In other words, inertial amplification is a critical concept to release the dependence of the low-frequency and broad bandgaps on low stiffness and bulky masses. However, numerous extended research ideas are limited to the classical models to slow or stall the advances in this problem [48-56]. The proposal of the Thomson scattering provides new insight into designing more phonon crystals with an inertial amplification effect.

Based on the Thomson scattering mechanism, this work proposes a single-phase planar torsional chiral phononic crystal to achieve a low-frequency and wide-band confinement. In contrast to previous works, we use a chiral lattice not because of its higher specific stiffness but because of its motion coupling. It is essential to state that our "kinematic coupling" is not the negative equivalent modulus but the coupling that allowed for Thomson scattering phenomena in elastodynamics. To generate destructive interferences, the chiral unit cell will be mirrored to be anti-chiral. Eventually, the anti-chiral super-unit cell can open a low-frequency and broad bandgap. In contrast to the conventional local resonance, this Thomson scattering lattice has a broader bandgap and nearly the same order of magnitude decay starting frequency for the same lattice constant, equivalent stiffness, and density conditions. The material damping can effectively suppress the high-frequency modes, so that the bandgap exhibits the effect of a low-pass filter rather than a band-stop filter in the axial chiral lattice.

The paper is organized as follows. Section 1 presents the background for planar chiral phononic crystals. In order to distinguish our design method from that based on local resonance and clear the superiority of this study, Section 2 is devoted to comparing classical local resonance-induced and Thomson scattering-induced planar chiral phononic crystals. Then, the design mechanism is discussed in Section 3. Section 4

presents a single-phase planar chiral phononic crystal with a more superior bandgap obtained according to the two-stage inertial amplification in the translation-rotation coupling system. Section 5 exhibits an experimental verification. Finally, Section 6 concludes the paper.

2. Design & Method

The low-frequency and broad bandgaps contradict equivalent physical parameters such as lattice constant, equivalent stiffness, equivalent density [44, 45]. For a fair comparison and to clarify the innovation of our study, we have embedded local resonance substructures and steel pillars in an identical chiral matrix to form a local resonance lattice (Fig. 1(a)) and a composite lattice (Fig. 1(b)) with equal weight. The minimum period of the local resonance (Fig. 1(a)) and the composite structures (Fig. 1(b)) is one-quarter of the lattices shown in Fig. 1. Thus, we named the geometries shown in Fig. 1(a) and Fig. 1(b) as super-unit cells. The local resonance unit cell (Fig. 1(a)) is composed of three materials, including the nylon with the elastic module E =1.6e9 Pa, density ρ =1000 kg/m^3, Poison's ratio v =0.4, the steel with the elastic module E =2.1e11 Pa, density ρ =7850 kg/m^3, Poison's ratio v =0.3, and the rubber with the elastic module E =5e6 Pa, density ρ =1000 kg/m^3, Poison's ratio v =0.47. The composite unit cell (Fig. 1(b)) is polluted from the local resonance lattice, where the rubber is replaced by nylon. The rubber has the same density as the nylon to ensure that the two lattices have the same mass. In addition to the outer circle diameter d_o=20 mm of the rubber, the two super-unit cells have the same other geometric parameters, including the lattice constant a =50 mm, the angle θ =30°, the width l = 10 mm and thickness t = 2.5 mm, and the parameters h =8.32 mm and d_i =12.4 mm. Therefore, the two lattices have the same equivalent density. The ligaments are more easily deformed compared to the lumped mass, so the equivalent stiffness of the lattice is mainly determined by the ligaments. Since both lattices have the same ligaments, both have a quasi-same equivalent stiffness.

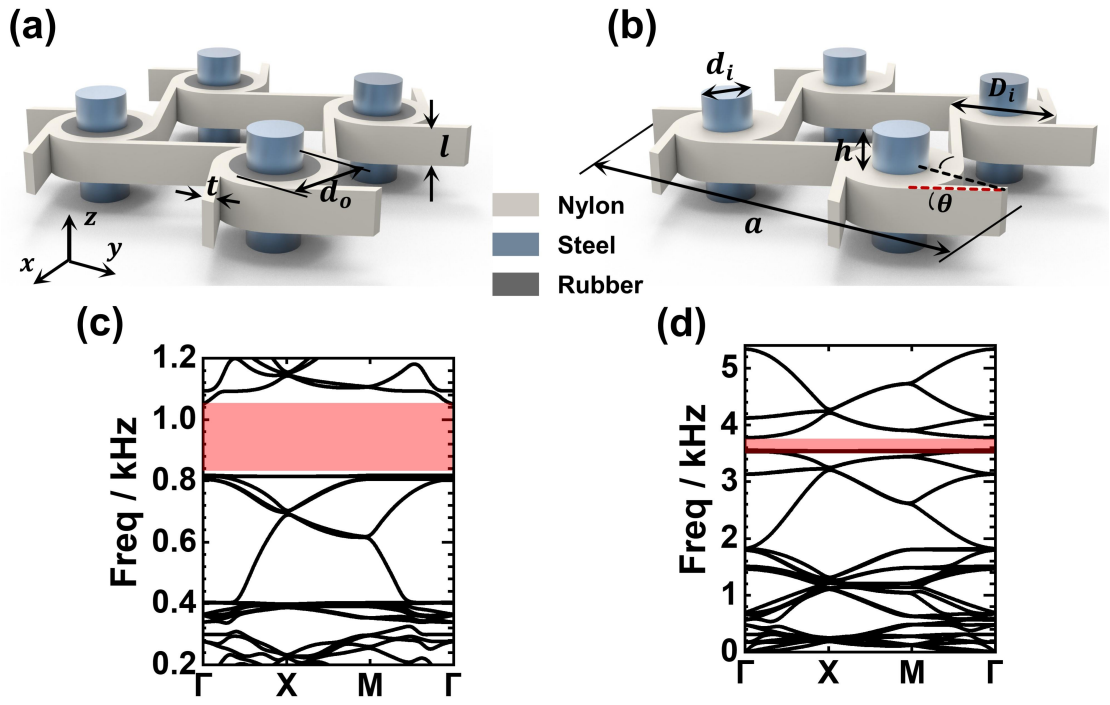

Fig. 1. (a)-(b) Schematics and (c)-(d) band structures of the arrayed local resonant super-unit cell and composite super-unit cell. The unit cell is one-quarter of the lattice.

Fig. 1(c) and Fig. 1(d) illustrate the band structures of the local resonance lattice (Fig. 1(c)) and composite lattice (Fig. 1(d)), which are obtained in the solid mechanic module of COMSOL Multiphysics through applying the Bloch periodic boundary [57] on the super-unit cell. It can be found that the local resonance bandgap extends from about 800 to 1050 Hz, while in the composite lattice, we have a narrow bandgap, i.e., 3540-3760 Hz. According to the relative width of the bandgap to evaluate the two unit cells [58], it is 27% of the local resonance unit cell and 6% of the composite structure. In short, the local resonance unit cell has better performance than the composite structure for both starting frequency and width of the bandgap.

To obtain the broad bandgap similar to that of Refs. [37, 40], it is indispensable to mirror unit cells shown in Fig. 1. The geometries of the mirrored super-lattices are presented in Fig. 2(a) and (b), and the band structures are shown in Fig. 2(c) and Fig. 2(d). One can observe that the bandgap of the local resonance extends from 700 to 1050 Hz. Compared with the previous results shown in Fig. 1(c), the lower boundary is shifted down by about 100 Hz, and the upper boundary is nearly invariable. Remarkably, for the composite super-unit cell, the narrow bandgap shown in Fig. 1(d) becomes a continuous and broad bandgap extending from 1600 to 5200 Hz, with the lower boundary significantly lowered from 3540 Hz to 1600 Hz.

To sum up, it is effective that mirroring improves the lower boundary of the local resonance bandgap. Still, the mirroring here is an optimization without changing the mechanism of the bandgap opening. Unlike in the local resonance super-unit cell, mirroring in the composite super-unit cell activates a new mechanism, thus resulting in a broad bandgap, which sets our study and approaches apart from the traditional design ideas.

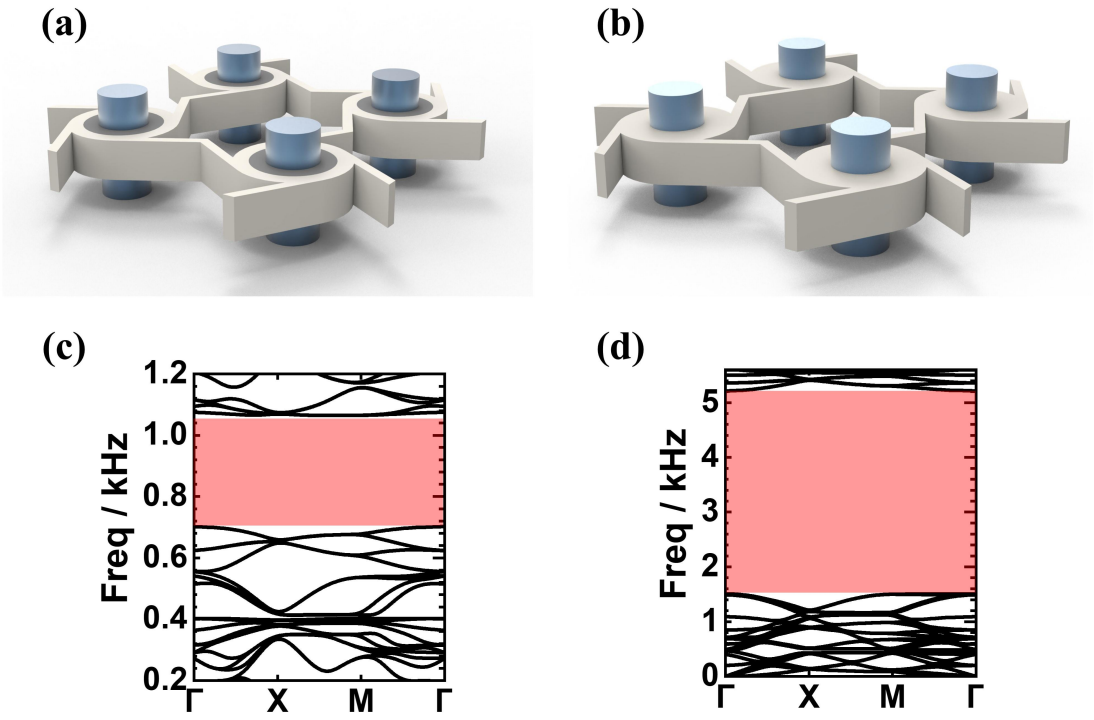

Fig. 2. (a)-(b) Schematics and (c)-(d) band structures of the mirrored local resonant super-unit cell and composite super-unit cell.

3. The mechanism of the bandgap opening

Statics can illustrate the polarization mode and direction of the LMs in dynamics in deep subwavelength [37, 59]. To understand the underlying physics, the static deformation of the mirrored super-unit cell (Fig. 3(a)) is computed numerically with COMSOL solid module. In the simulation, the material is linear, and geometric nonlinearity is not considered. As shown in Fig. 3, for easy differentiation, the first layer chiral units L_1 are numbered ① and ②, and the second layer L_2 are numbered ③ and ④. The nodes between the ① and ③ as well as the ② and ④ are defined as p_1 and p_2. Both upper and lower plates are considered as rigid, and the rest of the structure is defined as nylon. A force F along -y axis is applied at the top of the upper

plate and a fixed boundary condition is set at the lower plate.

In this chiral system, when the incident wave polarizing in translational harmonic motion goes through the first-layer unit cell L_1, the outgoing wave will have two polarizations, i.e., translation and rotation [37]. By analogy, each subsequent wave passing through a layer of chiral unit cells is equivalent to passing through Thomson scattering once more. Therefore, we defined that the first layer L_1 refers to the first Thomson scattering and the second layer L_2 refers to the second Thomson scattering [40].

Fig. 3(a) is the total deformation of the mirrored super-unit cell. One can observe from the deformation profiles that all chiral unit cells have significant translation along y-axis and rotation around the z-axis, as well as slight translation along x-axis. For ease of understanding, we ignore the translational motion in the x-axis in following discussion. The coupled phenomenon indicates that the unit cell has first two basic properties of Thomson scattering bandgap, i.e., two orthogonal motions and they are coupled on the same lumped mass. However, to realize the Thomson scattering bandgap, generating the opposite sub-motions in the same unit cell is crucial.

Although there is a significant reverse of the motion between the unit cells in L_1 and L_2, it is unclear whether the movements of the unit cells in L_1 can create opposite sub-motions in the same polarization of the unit cells in L_2. Consequently, for the sake of clarity, we have limited the z-axis rotational freedom and y-axis translational freedom of the L_1 unit cells separately to distinguish the polarized directions of the L_2 unit cells drived by the two types of motion of the L_1 unit cells.

Fig. 3(b) is the deformation profile when the rotation of L_1 is limited. In this condition, the unit cells ① and ② have only the translation along y axis. It can be found that nodes p_1 and p_2 will move along -y axis and close to each other. According to the movements of two nodes, from the perspective of the unit cells ③ and ④, the force direction of the node p_1 is denoted as the inset in the upper right of Fig. 3(b), and the ones of the node p_2 is presented as the inset in the lower right of Fig. 3(b). When the translational degrees of freedom of the layer L_1 are constrained, the deformation of the super-unit cell is shown in Fig. 3(c). For clarity, Fig. 3(d) shows the enlarged deformation profile of L_2, and the force directions of nodes p_1 and p_2 are illustrated in the right of Fig. 3(d). Comparing the force directions shown in Fig. 3(b) and Fig. 3(d), it can be found that the translation and rotation of the unit cells L_1 result in node

p_1 (or p_2) having opposite force directions, respectively. Because of the symmetry of the system, we can take unit cells ① and ③ as analytical objectives. Regarding the unit cell ① shown in Fig. 3(b), it will have the translation along -y axis and rotation around -z axis when it is compressed; conversely, it will produce the translation +y axis and rotation around +z axis when it is stretched. When unit cell ① has only translation, it will compress unit cell ③, at which time unit cell ③ will produce -y-axis translation and -z-axis rotation; when unit cell ① has only rotation, it will stretch unit cell ③, as a result, unit cell ③ will have +y-axis translation and +z-axis rotation. In other words, when unit cell ① is compressed, it has two polarizations, i.e., translation and rotation. Further, these two polarizations drive unit cell ③ have two sub-translations and two sub-rotations simultaneously. The most crucial is that these sub-motions of the unit cells L_2 vibrating in the same polarization have opposite directions. Consequently, the chiral twist super-unit cell shown in Fig. 3(a) satisfies the three conditions of generating Thomson scattering bandgap, i.e., two and more orthogonal motions coupled on the same lumped mass. After the second Thomson scattering, the sub-motions polarized in the same mode have opposite initial motion directions, which is the underlying mechanism by which this super-unit cell can achieve a low-frequency and wide bandgap.

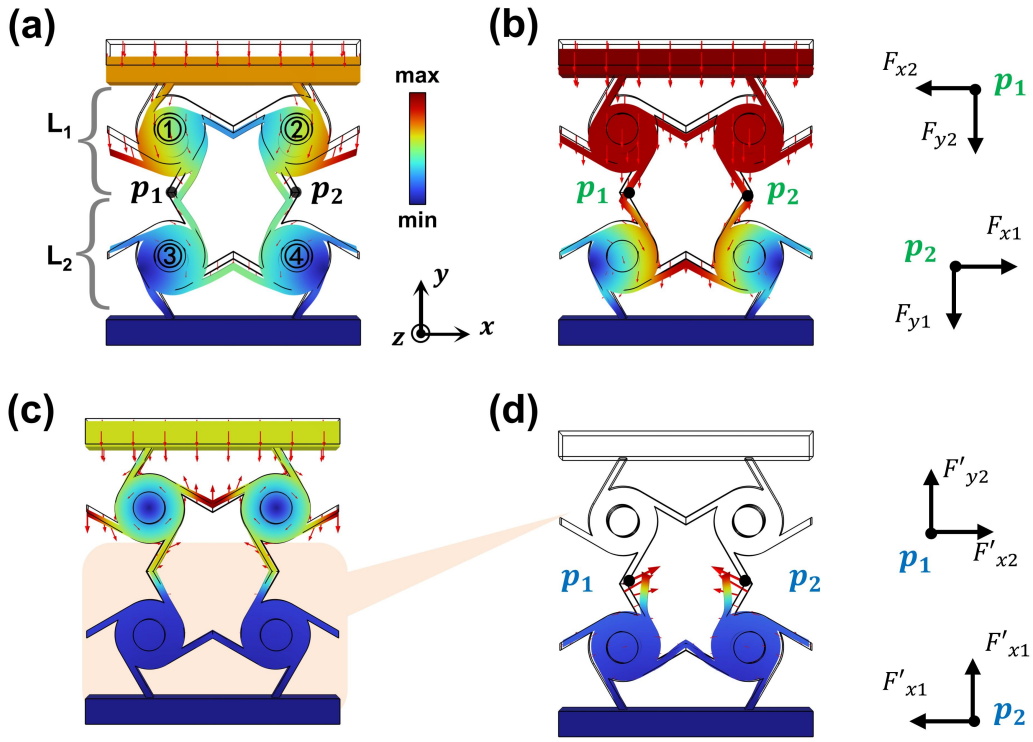

Fig. 3. Deformation profiles of the mirrored lattice under the condition of (a) free, (b) constrained z-axis rotation of the L_1, and (c) constrained y-axis translation of the L_1. (d) Enlargement of Fig. 3(c). The black wireframe is the original shape of the lattice. The red arrow points to the deformation direction.

The analytical approach was applied to the arrayed super-unit cell (in Fig. 4(a)) to clarify the difference between arrayed and mirrored super-unit cells. The arrayed super-unit cell is unstable because it produces shear motion along the x axis under the y-direction load. The unstable phenomenon can be observed from the animations in Supplementary information. To realize the same input displacement condition as the mirrored phononic crystal, the translational motion of the upper top plate in the x-direction is constrained in the calculation, while the other boundary conditions are the same as the ones applied on the mirrored super-unit cell.

Fig. 4(a) is the total static deformation profile. Different from Fig. 3(a), the deformation is asymmetric. Some unit cells have a significant rotation, such as unit cell ②, while some units do not have significant rotation, such as unit cell ①, even if both translation and rotation are feeble, such as unit cell ④. In more details, when the rotation of the unit cells L_1 around z axis is constrained, the deformation of the unit cells L_2 exhibits the same direction but to a different extent, as illustrated in Fig. 4(b). Also, when the rotation of the unit cells L_1 along -y axis is constrained, the deformation of

the unit cells L_2 exhibits the same direction but to a different extent as well, as illustrated in Fig. 4(c). The right insets of Fig. 4(b) and Fig. 4(d) show the force directions from the viewpoint of the unit cells L_2. One can observe that both nodes p_1 and p_2 have opposite force directions in the y-direction, which seems to mean that there are destructive interferences in the arrayed super-unit cell. However, the force direction in x-direction is identical. Because of the identical force direction, the super-unit cell has the asymmetric deformation, and some chiral unit cells have almost completely lost the coupled motion, which is one of the critical conditions for this bandgap generation. Consequently, the arrayed super-unit cell does not have the excellent bandgap of the mirrored super-unit cell, although both unit cells have the same equivalent density, lattice constant, and virtually identical stiffness and strength (Please refer to Fig. A1).

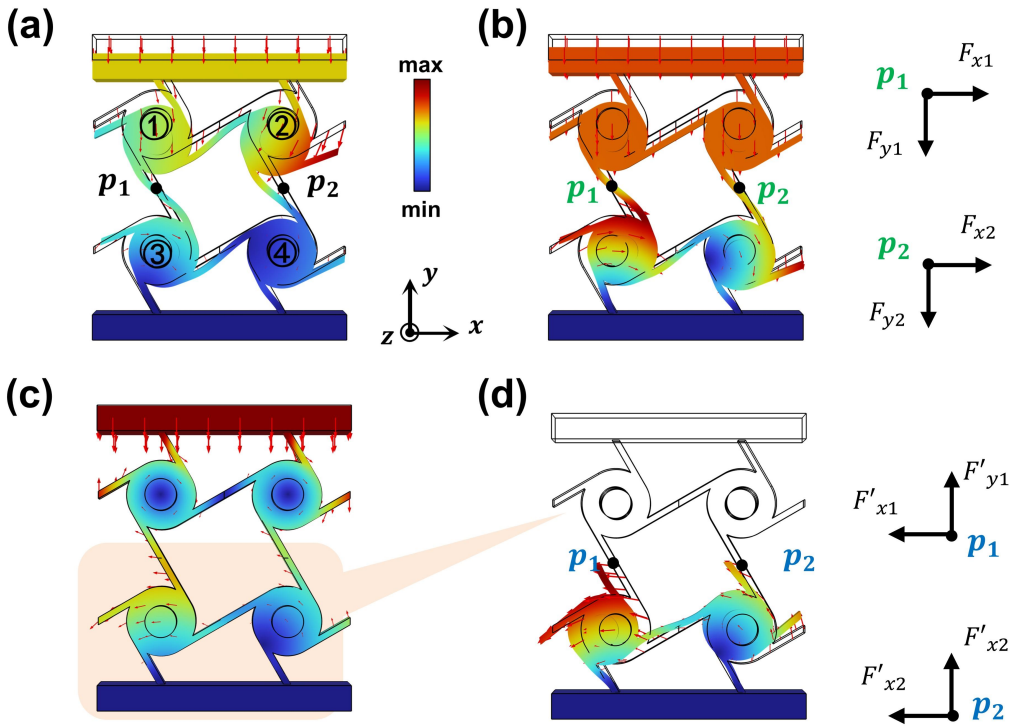

Fig. 4. Deformation profiles of the arrayed lattice under the condition of (a) free, (b) constrained z-axis rotation of the L_1, and (c) constrained y-axis translation of the L_1. (d) Enlargement of Fig. 4(c). The black wireframe is the original shape of the lattice. The red arrow points to the deformation direction.

4. Single-phase planar phononic crystal

Our previous study [40] has demonstrated that the coupling of the orthogonal motions

is analogous to Thomson scattering. During the quantitative description of the Thomson scattering based on the analytical formalism, the inertia matrix exhibits inertial amplification [40]. Interestingly, the involvement of the rotation allows the system to have two stages of inertial amplification, one of which depends on angle θ, and the other on the rotational inertia of lumped masses [46]. The larger the rotational inertial is, the lower the starting frequency of the bandgap is.

Regarding the composite structure shown in Fig. 2(b), it is not conducive to manufacturing and controlling the robustness of the elastic dynamics in practice [60]. Besides, steel, as a material with high density, is not suitable for obtaining large rotational inertia. To overcome these limitations, we propose a single-phase chiral unit cell composed of a matrix I and a lumped mass II, as shown in Fig. 5(a). The parameter $H = 2\hbar + l$ is designed to maintain the same height in z-axis as the composite unit cell. For the meshing in the numerical calculation, the diameter d_s is equal to $D_i - 2$ mm (please refer to Fig. 1(b) to find D_i). In order to use the rotational inertia of the lumped mass to generate a low starting frequency of the bandgap, while giving enough space for the dynamical deformation of the system, we set the diameter as D_o=0.5a -2 mm. Ultimately, for comparison purpose, the entire lattice (Fig. 5(a)) needs to have the same weight as the composite lattice (Fig. 1(b)), so γ = 20°. The super-unit cell shown in Fig. 5(b) can be obtained by mirroring the lattice III shown in Fig. 5(a). Fig. 5(c) is the band structure of the model exhibiting a broad bandgap within 965-5025Hz. Compared to the composite super-unit cell, the starting frequency is reduced from 1510 Hz to 965 Hz, with a decrease of 36%. The upper boundary of the bandgap is reduced from 5200 Hz to 5025 Hz. The relative width of the bandgap is improved from 110% to 135%. It is worth noting that these variations happened in the case of the same lattice constant, equivalent density, and stiffness.

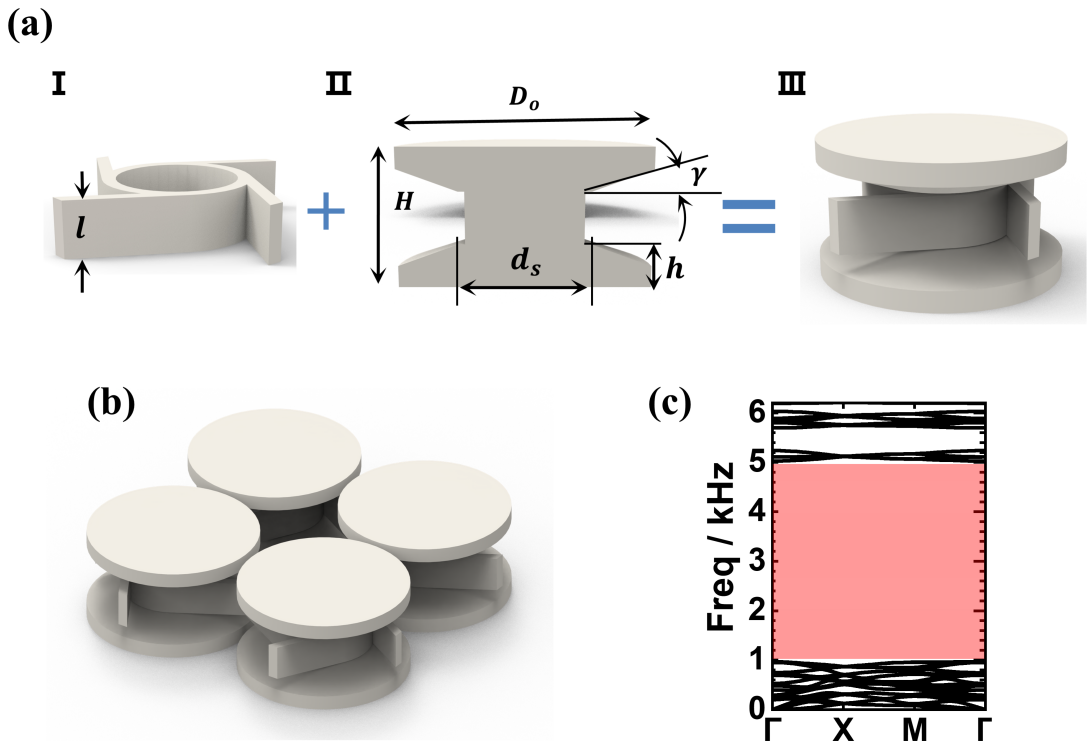

Fig. 5. (a) Schematics of the single-phase unit cell composed by I the matrix and II the lumped mass. (c) Band structure of the (b) mirrored unit cell.

5. Experimental verification and discussion

The FRFs of the finite structure (shown in Fig. 6 (a)), composed by 2×3 unit cells, is measured numerically and experimentally to validate the prediction of the created bandgap in the band structure. Two foams support the sample to levelling and isolate the vibration from the background [61]. A cubic block was designed at both the excitation end S_i and the output end S_o to facilitate the installation of the transducer and the excitation during the experiment. The same geometry is used in the simulation to minimize the differences between experiments and simulations. In the COMSOL V6.0 solid mechanics module, a harmonic excitation force F is applied to the input S_i, and the accelerations of S_i and S_o are recorded simultaneously by two domain point probes. The sweep frequency range covers 200 Hz to 7000 Hz with a frequency resolution of 5 Hz. The ratio of S_o to S_i is defined as the FRF. The experimental configuration (shown in Fig. 6) includes M+p Vibpilot, Modelshop K2007E01, and two acceleration transducers PCB353 B15.

The numerical and experimental results are illustrated in Fig. 6(b), where the blue plot corresponds to the simulation while the red plot to the experimental measurement. One can see that the attenuation of both results starts at about 710 Hz. The band gap type

can be determined from the distribution of energy within the bandgap. In Fig. 6(c), we have presented the deformation profiles at 3000 Hz. It can be found that the energy is mainly concentrated on the two lumped masses close to the source. In more detail, the vibration mode of the lumped masses is mainly rotational. According to the Thomson scattering mechanism, the attenuation relies mainly on the destructive interference formed during the second Thomson scattering, so the energy is mainly localized in the first layer of lumped masses, as presented in our previous work [40]. In other words, this bandgap belongs to the Thomson scattering type.

Compared to the numerical FRF of Fig. 6(b), there are some discrepancies between numerical and experimental results. Exceptionally, the depth of the experimental FRFs does not exceed 1e-4, which is because the output signal is already at the same level as the background noise. Besides, some numerical peaks close to 6200 Hz should belong to pass bands, but their attenuation coefficient approximates that of the bandgap in the experimental result. To find the reason, the deformation profile at 6250 Hz is shown in Fig. 6(d). It is clear that the resonant modes are the local resonance of the lumped masses. It has been demonstrated that damping in nylon is an effective approach to suppressing high-frequency local resonance modes [61, 62]. When the Rayleigh damping of α=0.1 s^{-1} and β= 4e-7 s [61, 62] is considered in simulation, as illustrated by the black dashed line in Fig. 6(b), the resonant peaks near 6250 Hz are compressed effectively, which is relative to a weak upward trend of the experimental result. In addition, manufacturing errors and the slight bending of the entire sample might be the causes of some peak shifts in experimental results, such as the difference between the numerical peak at 1750 Hz and experimental ones at 1400 Hz. Nevertheless, the consistent trend between the experiment and simulation can reveal the bandgap existence.

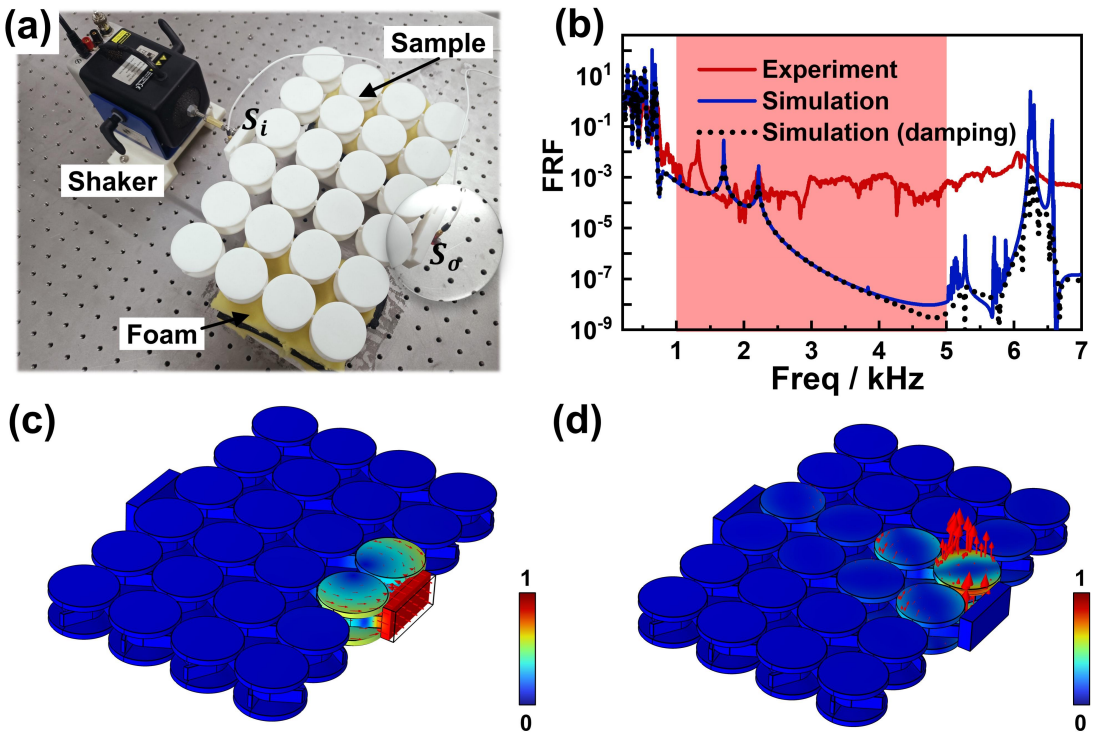

Fig. 6. (a) Photograph and configuration of the experiment. (b) Numerical and experimental FRFs. The red zone is the theoretical bandgap width predicted from the band structure. Deformation profiles at (c) 2968 Hz and (d) 6200Hz.

It is worth noting that the bandgap range predicted in the band structure is 965 Hz-5025 Hz. The attenuation range shown in FRF is 710 Hz-6220 Hz. The starting frequency of the attenuation in FRF is lower by about 250 Hz than that of the bandgap, with a relative difference of more than 25%. The cutoff of the bandgap is more than 1000 Hz higher than the prediction in band structure; the relative bandgap width is 135% in the bandgap, but the result is 159% in FRF.

To analyze the causes of the lower boundary differences, it is necessary to analyze the resonant modes from 710 Hz to 970 Hz located at the lower boundary of the bandgap. There are seven orders of passbands and three types of resonance modes. For simplicity, Fig. 7(a)-(c) show the three typical vibration modes (some repeated vibration modes are not mentioned). The first mode (in Fig. 7(a)) is the local deformation at the ligament; the second mode (in Fig. 7(b)) is the translation of the lumped mass in the z-axis; the third mode (in Fig. 7(c)) is the rotation of the lumped mass around an axis in the surface. Because these modes are orthogonal to the excitation direction, they cannot be effectively excited under the current excitation conditions.

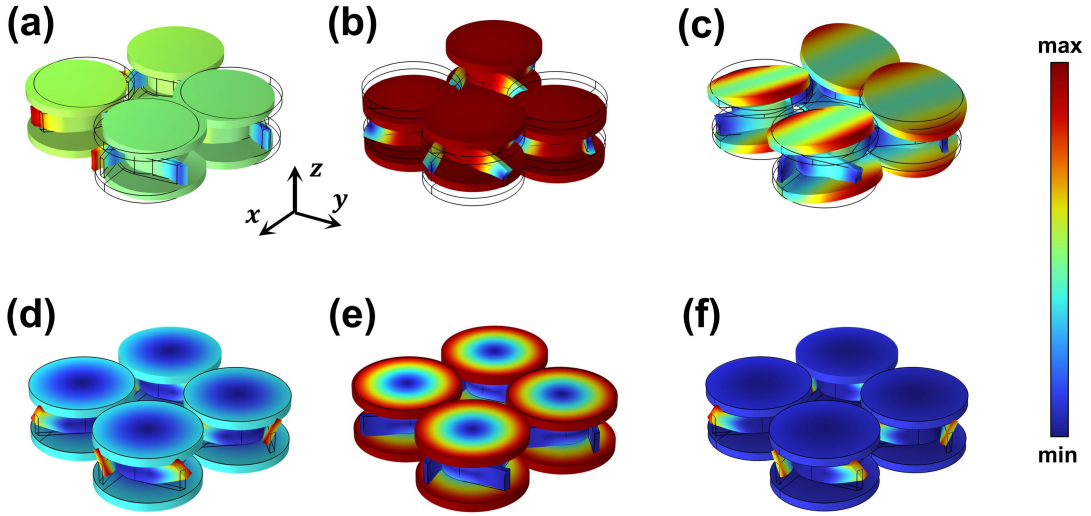

Fig. 7. (a)-(c) Three types of modes at the lower boundary (within 710–970 Hz) of the bandgap. (d)-(f) Three types of modes at the upper boundary (within approximately 5000-6100 Hz).

The upper boundary has a higher band spectrum density, but generally, it can be summarized as three patterns shown in Fig. 7(d)-(f), including the combined mode of the torsion of ligaments and rotation of the lumped mass (shown in Fig. 7(d)), the rotational mode of lumped masses around the z axis (shown in Fig. 7(e)), and the torsional mode of ligaments Fig. 7(f). Similar to low boundaries, the inability of these modes to effectively truncate the bandgap is due to orthogonality between the excitation direction and these modes.

In order to verify the above analysis, the out-of-plane input is applied in the simulation. The numerical results are shown in Fig. 8. It can be found that the attenuation starts at 1000 Hz and the cutoff frequency is 5000 Hz, which coincides with the prediction in band structure shown in Fig. 5(c). This analysis confirms the explanation that the attenuation width in the experimental FRF is wider than the energy band prediction.

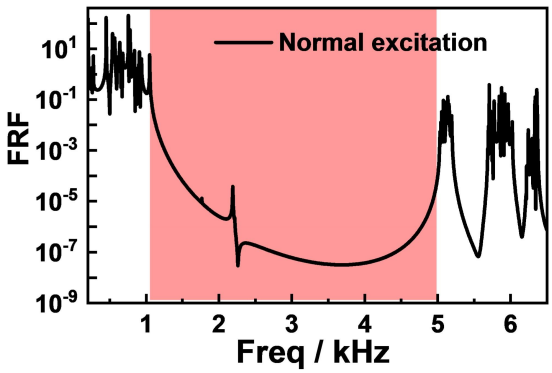

Fig. 8. Numerical FRF of the normal excitation. The red area refers to the bandgap width.

6. Conclusion

In summary, a single-phase planar chiral phononic crystal with a low-frequency and broad bandgap induced by Thomson Scattering has been proposed and investigated numerically and experimentally. Under the same lattice constant, stiffness and mass, the mirrored chirality only improves the width and starting frequency of the local resonance bandgap, while it can open a broad bandgap when the local resonant sub-structure is discarded. The superior bandgap performance depends on the Thomson scattering provided by translational and rotational coupling. According to the two-stage inertial amplification, we further simplified the material components of the unit cell and lowered the starting frequency of the bandgap as well, while the method is the changing in the appearance of the lumped masses only. The consequent result is that the starting frequency of the attenuation can be in the same order of magnitude as the local resonance bandgap and, moreover, the width is significantly better than the latter. Notably, different from the axially chiral phononic crystals whose bandgap exhibits band-pass filter properties, the blueprint carried out in this work has low-pass filtering properties due to the material damping. One cannot deny that the local resonance can generate a low-frequency bandgap due to the relevance between the starting frequency and the elastic module of the coating material [35, 63]. Of course, a new proposal in design may offer the possibility of increasing the inertial amplification factor, for the purpose of reducing the reliance on low stiffness and bulky masses for low-frequency and broad bandgaps [48]. These properties obtained in this work may make Thomson scattering a powerful approach and mechanism.

Appendix. A

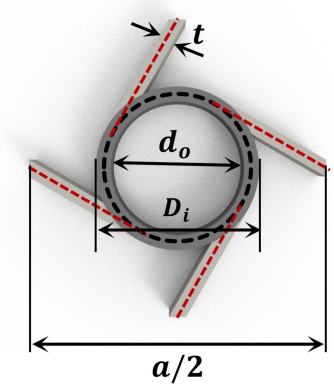

Fig. A1. Schematics of the ligaments. The red line is the symmetric line of the thickness, which is tangent to the black circle. Please note, the diameter of that circle is equal to $D_i - t$.

Appendix. B

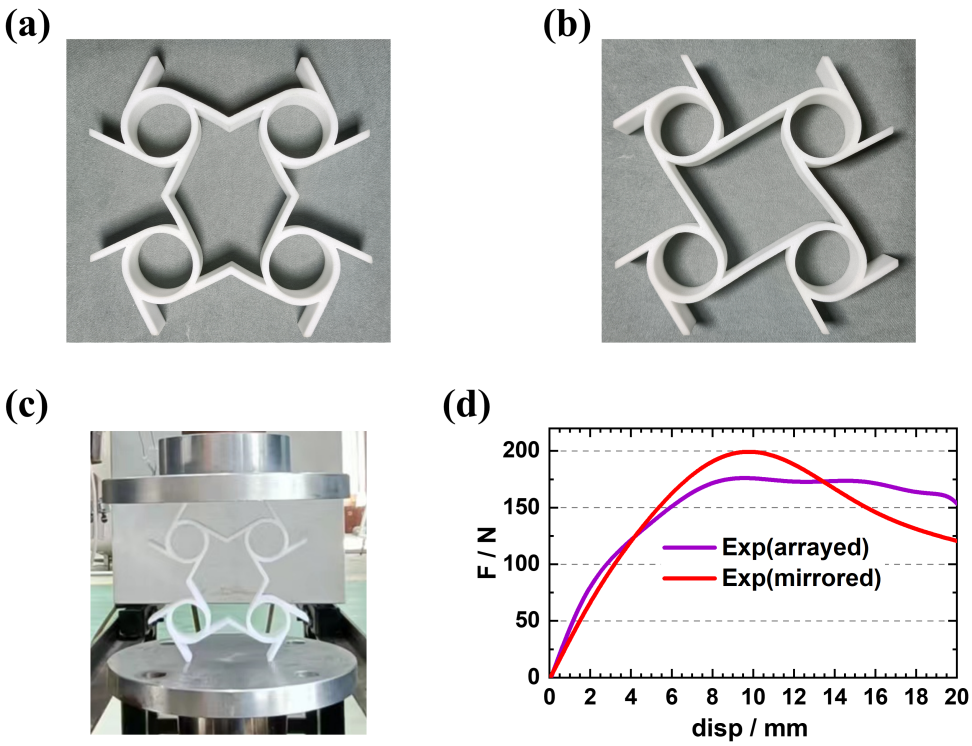

Fig. A2. The photographs of the mirrored lattice (a), arrayed lattice (b), and compression experiment (c). In order to ensure that the sample will not deform significantly in the normal direction during compression, the thickness l is 30 mm. Other geometric dimensions are the same as the matrix I Fig. 5(a). The universal testing machine is Instron 5982 and the loading speed is 2 mm/min. (d) The experimental results of the force-displacement curves.

Acknowledgments

This work was financially supported by the National Natural Science Foundation of China (Nos. 516750402 and 12002258)

Supplementary data

The data that support the findings of this study are available from the corresponding author upon reasonable request.

References

[1] V. Gold, Compendium of chemical terminology, International Union of Pure and Applied Chemistry, 528 (2014).

[2] H. Zhu, J. Yi, M.-Y. Li, J. Xiao, L. Zhang, C.-W. Yang, R.A. Kaindl, L.-J. Li, Y. Wang, X. Zhang, Observation of chiral phonons, Science, 359 (2018) 579-582.

[3] B. Kelvin, The Molecular Tactics of a Crystal, Clarendon Press, Oxford, 2012.

[4] R. Lakes, Foam Structures with a Negative Poisson's Ratio, Science, 235 (1987) 1038-1040.
[5] D. Prall, R.S. Lakes, Properties of a chiral honeycomb with a Poisson's ratio—1, Int.l J. Mech. Sci., 39 (1996) 305-314.
[6] R. Lakes, Deformation mechanisms in negative Poisson's ratio materials: structural aspects, Journal of Materials Science, 26 (1991) 2287-2292.
[7] A. Alderson, K.L. Alderson, D. Attard, K.E. Evans, R. Gatt, J.N. Grima, W. Miller, N. Ravirala, C.W. Smith, K. Zied, Elastic constants of 3-, 4- and 6-connected chiral and anti-chiral honeycombs subject to uniaxial in-plane loading, Composites Science and Technology, 70 (2010) 1042-1048.
[8] C.S. Ha, M.E. Plesha, R.S. Lakes, Chiral three-dimensional isotropic lattices with negative Poisson's ratio, Phys. Status Solidi B, 253 (2016) 1243-1251.
[9] M. Fu, F. Liu, L. Hu, A novel category of 3D chiral material with negative Poisson's ratio, Composites Science and Technology, 160 (2018) 111-118.
[10] R. Zhong, M. Fu, X. Chen, B. Zheng, L. Hu, A novel three-dimensional mechanical metamaterial with compression-torsion properties, Compos. Struct., 226 (2019) 111232.
[11] B.-B. Zheng, R.-C. Zhong, X. Chen, M.-H. Fu, L.-L. Hu, A novel metamaterial with tension-torsion coupling effect, Mater. Des., 171 (2019) 107700.
[12] T. Frenzel, M. Kadic, M. Wegener, Three-dimensional mechanical metamaterials with a twist, Science, 358 (2017) 1072-1074.
[13] A. Spadoni, M. Ruzzene, Elasto-static micropolar behavior of a chiral auxetic lattice, J. Mech. Phys. Solids, 60 (2012) 156-171.
[14] A. Spadoni, M. Ruzzene, S. Gonella, F. Scarpa, Phononic properties of hexagonal chiral lattices, Wave Motion, 46 (2009) 435-450.
[15] H. Nassar, Y.Y. Chen, G.L. Huang, Polar Metamaterials: A New Outlook on Resonance for Cloaking Applications, Phys. Rev. Lett., 124 (2020) 084301.
[16] G. Carta, I.S. Jones, N.V. Movchan, A.B. Movchan, Wave polarization and dynamic degeneracy in a chiral elastic lattice, Proc Math Phys Eng Sci, 475 (2019) 20190313.
[17] K. Zhang, Y. Su, P. Zhao, Z. Deng, Tunable wave propagation in octa-chiral lattices with local resonators, Compos. Struct., 220 (2019) 114-126.
[18] K. Zhang, P. Zhao, F. Hong, Y. Yu, Z. Deng, On the directional wave propagation in the tetrachiral and hexachiral lattices with local resonators, Smart Materials and Structures, 29 (2020).
[19] N. Karathanasopoulos, J.F. Ganghoffer, Chiral and non-centrosymmetric effects on the nonlinear wave propagation characteristics of architectured cellular materials, Waves in Random and Complex Media, (2020) 1-19.
[20] E. Baravelli, M. Ruzzene, Internally resonating lattices for bandgap generation and low-frequency vibration control, J. Sound Vib., 332 (2013) 6562-6579.
[21] F. Agnese, C. Remillat, F. Scarpa, C. Payne, Composite chiral shear vibration damper, Compos. Struct., 132 (2015) 215-225.
[22] R. Zhu, X.N. Liu, G.K. Hu, C.T. Sun, G.L. Huang, A chiral elastic metamaterial beam for broadband vibration suppression, J. Sound Vib., 333 (2014) 2759-2773.
[23] A. Bacigalupo, M.L. De Bellis, Auxetic anti-tetrachiral materials: Equivalent elastic properties and frequency band-gaps, Compos. Struct., 131 (2015) 530-544.
[24] A. Bacigalupo, G. Gnecco, M. Lepidi, L. Gambarotta, Optimal design of low-frequency band gaps in anti-tetrachiral lattice meta-materials, Compos. B. Eng., 115 (2017) 341-359.
[25] D. Qi, H. Yu, W. Hu, C. He, W. Wu, Y. Ma, Bandgap and wave attenuation mechanisms of innovative reentrant and anti-chiral hybrid auxetic metastructure,

Extreme Mech. Lett., 28 (2019) 58-68.
[26] Y. Li, G. Yan, Vibration characteristics of innovative reentrant-chiral elastic metamaterials, European Journal of Mechanics - A/Solids, 90 (2021) 104350.
[27] W. Wu, W. Hu, G. Qian, H. Liao, X. Xu, F. Berto, Mechanical design and multifunctional applications of chiral mechanical metamaterials: A review, Mater. Des., 180 (2019).
[28] D. Bigoni, S. Guenneau, A.B. Movchan, M. Brun, Elastic metamaterials with inertial locally resonant structures: Application to lensing and localization, Phys. Rev. B, 87 (2013).
[29] X.N. Liu, G.K. Hu, C.T. Sun, G.L. Huang, Wave propagation characterization and design of two-dimensional elastic chiral metacomposite, J. Sound Vib., 330 (2011) 2536-2553.
[30] Z. Liu, C.T. Chan, P. Sheng, Analytic model of phononic crystals with local resonances, Phys. Rev. B, 71 (2005) 014103.
[31] Y. Ding, Z. Liu, C. Qiu, J. Shi, Metamaterial with Simultaneously Negative Bulk Modulus and Mass Density, Phys. Rev. Lett., 99 (2007).
[32] R. Zhu, X.N. Liu, G.K. Hu, C.T. Sun, G.L. Huang, Negative refraction of elastic waves at the deep-subwavelength scale in a single-phase metamaterial, Nat. Commun., 5 (2014) 5510.
[33] A. Bacigalupo, L. Gambarotta, Simplified modelling of chiral lattice materials with local resonators, Int. J. Solids Struct., 83 (2016) 126-141.
[34] D. Mousanezhad, B. Haghpanah, R. Ghosh, A.M. Hamouda, H. Nayeb-Hashemi, A. Vaziri, Elastic properties of chiral, anti-chiral, and hierarchical honeycombs: A simple energy-based approach, Theoretical and Applied Mechanics Letters, 6 (2016) 81-96.
[35] Z. Liu, X. Zhang, Y. Mao, Y.Y. Zhu, Z. Yang, C.T. Chan, P. Sheng, Locally Resonant Sonic Materials, Science, 289 (2000) 1734-1736.
[36] H.H. Huang, C.T. Sun, Wave attenuation mechanism in an acoustic metamaterial with negative effective mass density, New J. Phys., 11 (2009) 013003.
[37] A. Bergamini, M. Miniaci, T. Delpero, D. Tallarico, B. Van Damme, G. Hannema, I. Leibacher, A. Zemp, Tacticity in chiral phononic crystals, Nat. Commun., 10 (2019) 4525.
[38] B. Zheng, J. Xu, Mechanical logic switches based on DNA-inspired acoustic metamaterials with ultrabroad low-frequency band gaps, J. Phys. D: Appl. Phys., 50 (2017) 465601.
[39] A.H. Orta, C. Yilmaz, Inertial amplification induced phononic band gaps generated by a compliant axial to rotary motion conversion mechanism, J. Sound Vib., 439 (2019) 329-343.
[40] W. Ding, T. Chen, C. Chen, D. Chronopoulos, B. Assouar, J. Zhu, Experimental Observation and Description of Bandgaps Opening in Chiral Phononic Crystals by Analogy with Thomson scattering, Preprint doi:10.48550/arxiv.2207.04282, (2022).
[41] C. Yilmaz, G.M. Hulbert, Theory of phononic gaps induced by inertial amplification in finite structures, Phys. Lett. A, 374 (2010) 3576-3584.
[42] C. Yilmaz, G.M. Hulbert, N. Kikuchi, Phononic band gaps induced by inertial amplification in periodic media, Phys. Rev. B, 76 (2007) 054309.
[43] C. Yilmaz, N. Kikuchi, Analysis and design of passive low-pass filter-type vibration isolators considering stiffness and mass limitations, J. Sound Vib., 293 (2006) 171-195.
[44] A.S. Phani, J. Woodhouse, N.A. Fleck, Wave propagation in two-dimensional periodic lattices, J. Acous. Soc. Am., 119 (2006) 1995-2005.

[45] T. Delpero, G. Hannema, B.V. Damme, S. Schoenwald, A. Zemp, A. Bergamini, Inertia Amplification in Phononic Crystals for Low Frequency Band Gaps, in: VIII ECCOMAS Thematic Conference on Smart Structures and Materials SMART 2017, 2017, pp. 1657-1668.
[46] W. Ding, T. Chen, C. Chen, D. Chronopoulos, J. Zhu, A three-dimensional twisted phononic crystal with omnidirectional bandgap based on inertial amplification by utilizing translation-rotation coupling, J. Sound Vib., 541 (2022) 117307.
[47] N.M.M. Frandsen, O.R. Bilal, J.S. Jensen, M.I. Hussein, Inertial amplification of continuous structures: Large band gaps from small masses, J. Appl. Phys., 119 (2016) 124902.
[48] J. Li, P. Yang, S. Li, Phononic band gaps by inertial amplification mechanisms in periodic composite sandwich beam with lattice truss cores, Compos. Struct., 231 (2020) 11458.
[49] C. Xi, L. Dou, Y. Mi, H. Zheng, Inertial amplification induced band gaps in corrugated-core sandwich panels, Compos. Struct., 267 (2021) 113918.
[50] J.U. Schmied, C. Sugino, A. Bergamini, P. Ermanni, M. Ruzzene, A. Erturk, Toward structurally integrated locally resonant metamaterials for vibration attenuation, in, SPIE, 2017.
[51] M. Barys, J.S. Jensen, N.M.M. Frandsen, Efficient attenuation of beam vibrations by inertial amplification, European Journal of Mechanics - A/Solids, 71 (2018) 245-257.
[52] J. Li, S. Li, Generating ultra wide low-frequency gap for transverse wave isolation via inertial amplification effects, Phys. Lett. A, 382 (2018) 241-247.
[53] F. Zeighami, A. Palermo, A. Marzani, Inertial amplified resonators for tunable metasurfaces, Meccanica, 54 (2019) 2053-2065.
[54] J. Zhou, L. Dou, K. Wang, D. Xu, H. Ouyang, A nonlinear resonator with inertial amplification for very low-frequency flexural wave attenuations in beams, Nonlinear Dynamics, 96 (2019) 647-665.
[55] J. Li, P. Yang, S. Li, Multiple band gaps for efficient wave attenuation by inertial amplification in periodic functionally graded beams, Compos. Struct., 271 (2021).
[56] O. Yuksel, C. Yilmaz, Realization of an ultrawide stop band in a 2-D elastic metamaterial with topologically optimized inertial amplification mechanisms, Int. J. Solids Struct., 203 (2020) 138-150.
[57] H. Chen, H. Nassar, G.L. Huang, A study of topological effects in 1D and 2D mechanical lattices, J. Mech. Phys. Solids, 117 (2018) 22-36.
[58] S. Taniker, C. Yilmaz, Generating ultra wide vibration stop bands by a novel inertial amplification mechanism topology with flexure hinges, Int. J. Solids Struct., 106-107 (2017) 129-138.
[59] R.C. Hibbeler, Engineering Mechanics: Statics & Dynamics, 14 ed., Prentice Hall, New Jersey, 2015.
[60] K.H. Matlack, A. Bauhofer, S. Krödel, A. Palermo, C. Daraio, Composite 3D-printed metastructures for low-frequency and broadband vibration absorption, Proc. Natl. Acad. Sci. U.S.A., 113 (2016) 8386-8390.
[61] L. D'Alessandro, E. Belloni, R. Ardito, A. Corigliano, F. Braghin, Modeling and experimental verification of an ultra-wide bandgap in 3D phononic crystal, Appl. Phys. Lett., 109 (2016) 221907.
[62] L. D'Alessandro, E. Belloni, R. Ardito, F. Braghin, A. Corigliano, Mechanical low-frequency filter via modes separation in 3D periodic structures, Appl. Phys. Lett., 111 (2017) 231902.
[63] K. Mizukami, T. Kawaguchi, K. Ogi, Y. Koga, Three-dimensional printing of

577 locally resonant carbon-fiber composite metastructures for attenuation of broadband
578 vibration, Compos. Struct., 255 (2021) 112949.
579